Influence of sintering temperature on the structural, electrical and microwave properties of yttrium iron garnet (YIG)

Article *in* Journal of Materials Science: Materials in Electronics · May 2018

DOI: 10.1007/s10854-018-8850-5

Influence of sintering temperature on the structural, electrical and microwave properties of yttrium iron garnet (YIG)

R. S. Azis, M. M. Syazwan, N. M. M. Shahrani, A. N. Hapishah, R. Nazlan, F. M. Idris, I. Ismail, M. M. M. Zulkimi, I. R. Ibrahim

Journal of Materials Science: Materials in Electronics

ISSN 0957-4522

J Mater Sci: Mater Electron
DOI 10.1007/s10854-018-8850-5

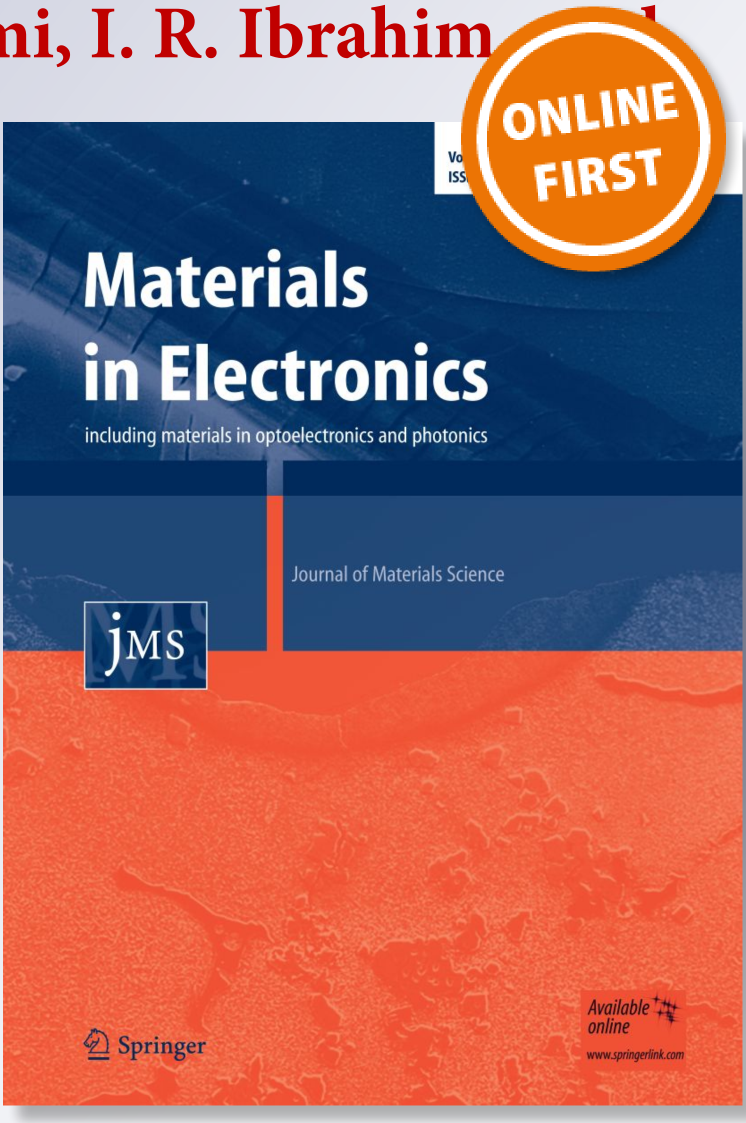

Springer

Journal of Materials Science: Materials in Electronics
https://doi.org/10.1007/s10854-018-8850-5

Influence of sintering temperature on the structural, electrical and microwave properties of yttrium iron garnet (YIG)

R. S. Azis[1,2] · **M. M. Syazwan**[2] · **N. M. M. Shahrani**[2] · **A. N. Hapishah**[2] · **R. Nazlan**[2,3] · **F. M. Idris**[2] · **I. Ismail**[2] · **M. M. M. Zulkimi**[2] · **I. R. Ibrahim**[2] · **Z. Abbas**[1,2] · **N. M. Saiden**[1]

Received: 5 January 2018 / Accepted: 1 March 2018

Abstract

This study investigates the structural, electrical and microwave properties of yttrium iron garnet (YIG) which focuses on the parallel evolving relationship with their dependence on the sintering temperature. The iron oxide obtained from the steel waste product (mill scale) was used to synthesize YIG. The raw mill scale underwent the milling and Curie temperature separation technique to produce high purity iron oxide powder which is the main raw material in preparing and fabricating YIG through high energy ball milling (HEBM) process. Microstructural features such as amorphous phase, grain boundary, secondary phase and intergranular pores contribute significantly to the additional magnetic anisotropy and demagnetizing fields, affecting the electric and microwave properties accordingly. The increment in electrical resistivity and decrement in linewidth while the microstructure was evolving is believed to be a strong indicator of improved phase purity and compositional stoichiometry.

1 Introduction

Yttrium iron garnet (YIG, $Y_3Fe_5O_{12}$) is extensively studied due to its specific magnetic and magneto-optical properties such as high quality factor in the microwave regime, small linewidth in magnetic resonance, and wide-ranging applications in magneto-optical and microwave communication fields such as optical isolators, circulators, and phase shifters [1–5]. The first known method in producing YIG was developed through the mixed oxides method or later known as the solid-state reaction method. However, high temperature was a requirement in this process [6]. Eventually, other synthesizing techniques were introduced such as microwave-assisted conventional ceramic approaches, co-precipitation, sol–gel, spray drying, freeze dying, combustion synthesis or glass crystallization [7–10]. It is notable that the best way to produce a single phase YIG (of high purity) with high density would possibly require expensive and high-end technology such as CVD and PVD [11]. However, to develop materials at a cheaper cost that use a simple technique, the solid-state method is still an attractive method to be employed [12, 13] although high processing temperature is a must. Furthermore, to meet the sintering requirements, powders prepared by this method need prolonged grinding which has the tendency to reduce the purity of the material. The final product, in this case, contains particles with large grain sizes (several micrometers) and a limited degree of homogeneity. Nevertheless, high sintering temperatures (> 1450 °C) and long soaking time (> 10 h) are required to produce YIG ferrite ceramics with a density of 97% for device applications. Therefore, it is important to produce garnets with a strict control of the composition, homogeneity, size and particle shape. In the past decades, studies on YIG by pure materials were reported in ferrite literature. However, the fabrication of YIG ferrite by using recycled steel waste product (mill scale) is still absent in the literature. Steel waste products were collected from the steel industry in order to produce iron oxide via the purification process. Iron oxide has high content of iron (Fe) and this had posed a challenge in purifying and recycling the iron oxide powder to produce YIG ferrites with low cost ferrite fabrication from the waste materials. Ferrite magnetic materials are known to be very dependable on their

---

R. S. Azis
rabaah@upm.edu.my

[1] Department of Physics, Faculty of Science, Universiti Putra Malaysia (UPM), 43400 Serdang, Selangor, Malaysia

[2] Materials Synthesis and Characterization Laboratory, Institute of Advanced Technology, Universiti Putra Malaysia (UPM), 43400 Serdang, Selangor, Malaysia

[3] Faculty of Industrial Sciences & Technology, Universiti Malaysia Pahang, Lebuhraya Tun Razak, 26300 Gambang Kuantan, Pahang, Malaysia

microstructure. YIG is known used for microwave device applications because it can be used at room temperature. YIG has proved to be a very useful material in microwave application because of their low resonance linewidth and high quality factor. Ferromagnetic resonance (FMR) is a very powerful and well-established dynamic technique to investigate magnetic materials and to determine magnetic properties. FMR absorption experiments measure the microwave power absorbed by a specimen as a function of an applied dc magnetic field (H). The resulting curve is described by a resonance field, H_{res} that corresponds to maximum power absorption, and by an absorption linewidth, ΔH. In this work, a series of low to high sintering temperature was used to obtain polycrystalline YIG powder. The phase evolution during the processing, and the sintering ability towards structural, electrical and microwave properties of sintered specimens are determined and discussed in detail.

2 Methodology

2.1 Preparation of hematite (Fe_2O_3)

Mill scale was collected from the steel factories in Malaysia. Impurities such as pieces of metal and brick, dirt, sand and oil—which covered the mill scale were removed during the mill scale selection. The evaluation of the physical condition of the mill scale was carried out by a visual inspection and followed by a sonication for 45 min. 100 g of mill scale was weighed using a digital weighing balance scale. The mill scale was then crushed through a wet milling process for 48 h to obtain a precise powder size. The as-milled powder was dessicated before magnetic separation processes were conducted. The magnetic particles were poured into a glass tube filled with 90–100 °C distilled water with the presence of 1 T external field. Due to the weak susceptibility of ferromagnetic particles, FeO (wustite) presumably would drop to the bottom of the tube, and the Fe_3O_4 (magnetite) and Fe_2O_3 (hematite) would be attracted to the surface close to the poles. This separation was sorted out based on the Curie temperature of FeO, Fe_2O_3 and Fe_3O_4 particles [14]. The particles that had been used for Fe_2O_3 production were the bottom particles. The powder then was oxidized using a furnace at 500 °C for 9 h in the air. The yield of oxidation, Fe_2O_3 was sieved to obtain a fine powder, and this was used as a raw material in preparing yttrium iron garnet (YIG).

2.2 Preparation of yttrium iron garnet (YIG)

The production method begins with the weighing of the oxides according to the stoichiometric ratio based on the equilibrium Eq. 1:

$$5Fe_2O_3 + 3Y_2O_3 \rightarrow 2Y_3Fe_5O_{12}. \tag{1}$$

In this process, the yttrium oxide (Y_2O_3) powder with 99.9% Alfa Aesar and Fe_2O_3 derived from mill scale were weighed and mixed using an agate mortar for approximately 1 h. The mixing powder was then milled using high energy ball mill with the ratio of 10:1 for 9 h. High energy ball milling was carried out at room temperature using hardened steel vials and steel balls. After milling, polyvinyl alcohol with 1 wt% PVA was added into the powder as a binder to provide strength to the pressed compact, and it was also lubricated with 0.3 wt% of zinc stearate. The as-milled powders were pressed uniaxially into toroidal form in a die with the diameter of 10 and 18 mm, respectively at about 3 MPa. Multi-samples sintering scheme was employed in which the sample was sintered from 500 °C up to 1400 °C with an increment of 100 °C for 9 h with the heating rate of 3 °C/min in ambient air atmosphere. The phases of the YIG samples were collected with X-ray diffraction (Phillips Expert Pro PW3040) using Cu-K_α radiation. The microstructure of the bulk samples was observed by using a FEI Nova NanoSEM 230 scanning electron microscope. The IR spectra of the samples were determined by using Thermo Scientific Nicolet 6700 IR spectrometer with the frequencies between 4000 and 400 cm^{-1}. The Raman characterization is performed by Witec Raman spectrometer model Alpha 300R with laser wavelength of 633 nm. The electrical resistivity of the sample was measured at room temperature from current the I value of the sample which was acquired using a Keithley 6485 Picoammeter. The samples were placed between a parallel plates and attached to the instrument. A current passed through the sample by a conducting metallic contact deposited at each sample's surface. A silver paste was deposited on each sample's toroidal surface after a smooth polish using silicon carbide paper. This will produce a better electrical connection between the samples and the plates. The sample's resistivity was measured using Eq. (2):

$$\rho = \frac{RA}{l} \text{ cm} \tag{2}$$

where R, A, and l being are the sample's electrical resistance, cross-section area, thickness.

The ferromagnetic resonance (FMR) linewidth of the sample was carried out by Agilent Technologies PNAN5227 Vector network analyzer (VNA). The VNA–FMR measurement operated at C band (4–8 GHz) frequency range and FMR parameters yields from standard microwave S—parameter measurements versus frequency and field (H). The measurement was carried out at varies the microwave frequency at a fixed static field, extracts the FMR absorption profile from standard S parameter measurements, and obtains a FWHM frequency swept linewidth from the response. The density of the sintered sample was obtained using the Archimedes principle with water as the fluid medium [15–20].

3 Results and discussions

The evolutions of phase formation of YIG for as-milled, and after sintering at 500–1400 °C with 100 °C increment were shown through the XRD spectrum in Fig. 1. The XRD pattern, corresponding to 9 h milling time, showed the peaks of starting oxide, Fe_2O_3 with no Y_2O_3—detected in the XRD pattern. The disappearance of peak Y_2O_3 was attributed to the milling process which implies that it had a faster fragmentation rate relative to Fe_2O_3. This suggests that the un-reacted Y_2O_3 in the mixture formed thin coating layers around Fe_2O_3 nanoparticles that were undetectable by XRD. This is consistent with the work in the reported literature [21]. The XRD, after the sintering temperature of 500 °C showed the peaks of starting oxide: Fe_2O_3 at $2\theta = 33.218°$ and Y_2O_3 at $2\theta = 29.150°$. The signature peaks of two starting materials, Fe_2O_3 and Y_2O_3 were indexed to ICDD reference code of 98-000-6274 and 98-000-8030, respectively. It could be observed that no reaction between the starting powders occurred prior to sintering as well as after sintering at 500 °C. At lower temperature of 500 °C, the particles of Fe_2O_3 and Y_2O_3 did not have enough energy to collide with each other. Thus, the rate of reaction at 500 °C was lower. The reaction only started after sintering at 600 °C through the formation of yttrium ferrite with perovskite structure ($YFeO_3$, ICDD: 98-004-8662, orthoferrite). It can be concluded that high energy milling can lead to the formation of minute amounts of orthoferrite and lower the temperature of orthoferrite formation [22]. The XRD pattern of the powder heat treated at 600 °C showed Y_2O_3, Fe_2O_3 and $YFeO_3$ phases with low amount of orthoferrite. After sintering at 700–800 °C, the sample readily gave diffraction peaks of $YFeO_3$ phase together with Fe_2O_3 and Y_2O_3 phases. The orthoferrite phase, $YFeO_3$ became the major phase. For the powder heat treated at 900 °C, it could be observed that Fe_2O_3 and Y_2O_3 disappeared; however, some garnet phase begin to appear, and by increasing the heat treatment temperature to 1000 °C, the garnet phase became the major phase and a little orthoferrite phase still remained.

The XRD pattern at the powder sintered at 1100 °C and above showed clear peaks matched with the cubic YIG phase (ICDD: 98-003-5954). The presence of the complete YIG phase can be indexed to (400), (420), (422), (521), (611), (444), (640), (642), (741), (840), (842), and (664) planes of a cubic unit cell. This indicates that the sintering temperature at 1100 °C can assist in obtaining YIG phase prepared by mechanical alloying method. This method is useful to promote the synthesis of nanostructured ferrite by mechanical activation of oxide compound. The XRD pattern showed that the peak of the phase had

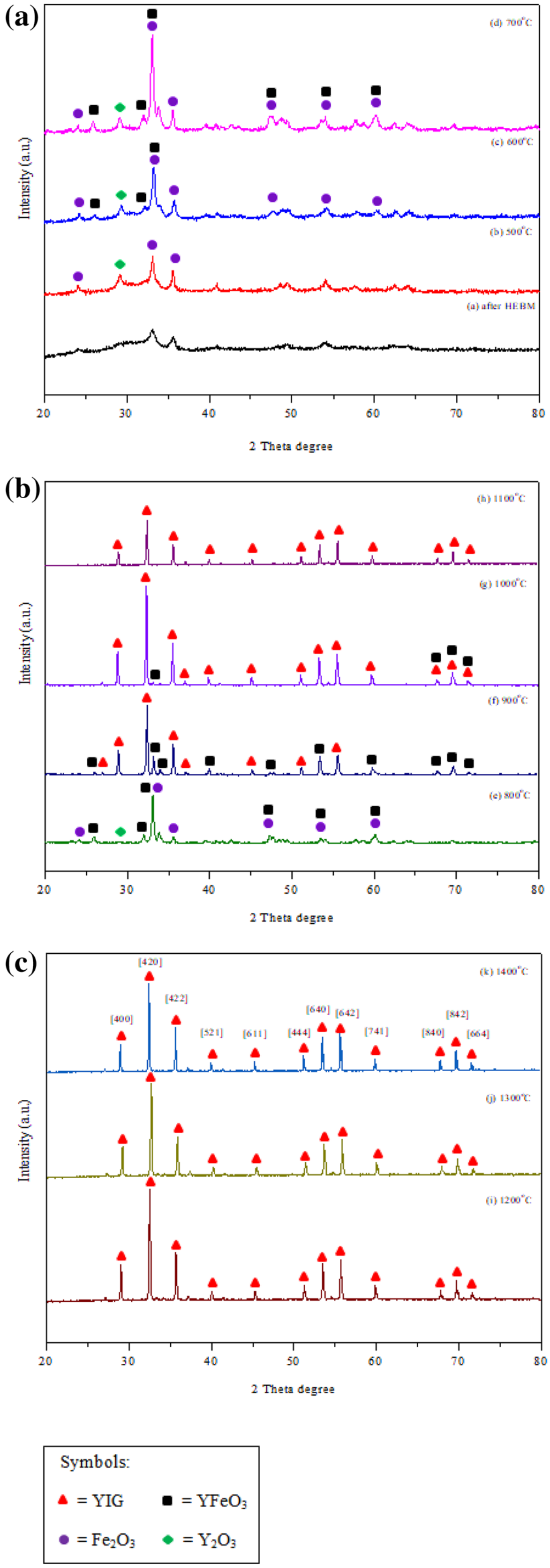

Fig. 1 XRD pattern of YIG sintered at **a** before sintering to 700 °C, **b** 800–1100 °C and **c** 1200–1400 °C

become narrower as a consequent of the increment of sintering temperature, suggesting improvement in the degree of crystallinity of the sintered samples. The intensity (peak height) for the phase increased after sintering at 500–1000 °C, and decreased for the heat treatment at 1100 °C. The fall in the XRD peak height at 1100 °C was not related to the crystallinity of the sample. The fall at 1100 °C was possibly due to the changes in the composition (stoichiometry) of the material. However, it is confirmed that by the XRD spectrum (Fig. 1), the YIG phase was complete at the temperature of 1100 °C.

Table 1 shows the details of XRD of the intense peaks before sintering, which represents the milling for 9 h, and at different sintering temperature. The XRD showed that after the milling process, the peak that gave the highest intensity belonged to the *R-3c* group of hematite. The same occurrence could be seen for the sample after sintering at 500 °C. The sample for sintering at 600–800 °C showed the presence of the space groups *R-3c* and *pnma* at the most intense peak. Those groups referred to the hematite and $YFeO_3$ phase. It can be stated that major hematite and orthoferrite phases were dominant for this temperature before the formation of the YIG phase. The YIG phase is dominant for sintering temperature at 900–1400 °C as the space group that belongs to the YIG phase is *la3d*. In spite of that, it could be seen that as the sintering temperature increased, the peak position from 500 to 600 °C increased too as the reaction started to form at 600 °C. The decreasing of peak position after sintering at 600–1000 °C was attributed to the transition of the orthoferrite phase to the YIG phase. After sintering at 1000–1300 °C, the peak position increased. This can be completely associated with the change to the YIG phase. The decreasing of the peak position at 1400 °C was due to the oxygen loss at higher temperature.

The density, relative density and porosity of the sintered samples at different sintering temperature are recorded in Table 2. The density of the sample is in the range of 4.670–5.111 g cm^{-3} with relative density of 90.319–98.859%. Relative density is calculated based on Eq. 3 [23]:

$$\text{Re lative density, } \rho_r = \left(\frac{\rho_{\text{exp}}}{\rho_{xrd}}\right) \times 100\% \tag{3}$$

where $_{exp}$ is an experimental density determined from Archimedes principle and ρ_{xrd} is a theoretical X-ray density (5.17 g cm^{-3}).

Table 2 Density, relative density and porosity at sintering temperature of 500–1400 °C

Sintering temperature (°C)	Density (g cm^{-3})	Relative density (%)	Porosity (%)
500	4.670	90.319	9.681
600	4.729	91.464	8.536
700	4.756	91.998	8.002
800	4.762	92.103	7.897
900	4.794	92.729	7.271
1000	4.806	92.967	7.033
1100	4.880	94.387	5.613
1200	4.890	94.576	5.424
1300	4.936	95.476	4.524
1400	5.111	98.859	1.141

Table 1 XRD details of the intense peaks before sintering and after sintering from 500 to 1400 °C

Sintering temperature (°C)	*hkl*	Phase	%	Space group	Peak position (°)	FWHM (°)	*a* (Å)
Before sintering	104	Fe_2O_3	100	*R-3c*	33.091	0.6336	5.038
500	104	Fe_2O_3	84	*R-3c*	33.128	0.1948	5.038
	222	Y_2O_3	16	*la-3*	29.199	0.2598	10.604
600	104	Fe_2O_3	50	*R-3c*	33.259	0.2273	5.038
	121	$YFeO_3$	43.3	*pnma*	33.259	0.2273	5.596
	222	Y_2O_3	7.0	*la-3*	29.304	0.2598	10.604
700	104	Fe_2O_3	50	*R-3c*	33.093	0.2598	5.038
	121	$YFeO_3$	44	*pnma*	33.093	0.2598	5.596
	222	Y_2O_3	6.0	*la-3*	27.170	0.3572	10.604
800	104	Fe_2O_3	50	*R-3c*	33.055	0.2273	5.038
	121	$YFeO_3$	47	*pnma*	33.055	0.2273	5.596
	222	Y_2O_3	3	*la-3*	29.076	0.3897	10.604
900	024	YIG	100	*la-3d*	32.354	0.1299	12.375
1000	024	YIG	100	*la-3d*	32.275	0.1188	12.375
1100	024	YIG	100	*la-3d*	32.368	0.1980	12.375
1200	024	YIG	100	*la-3d*	32.474	0.1188	12.375
1300	024	YIG	100	*la-3d*	32.649	0.1584	12.375
1400	024	YIG	100	*la-3d*	32.397	0.1188	12.375

The porosity of the sample is calculated using the Eq. 4:

$$\text{Porosity, } P = \left[1 - \left(\frac{\rho_{\exp}}{\rho_{xrd}}\right)\right] \times 100\% \qquad (4)$$

where $_{exp}$ is the experimental density of the sample and ρ_{xrd} is the XRD density.

Table 2 shows that the porosity decreased with the increment of the sintering temperature, while the density of the sample increased. During the sintering process, a driving force is generated due to the thermal energy produced by increasing the sintering temperature. This causes particles to move closer and grains to be formed by the movement of grain boundaries to grow over pores; this resulted in the decrement in the porosity and increment in the density of the sample. The driving force depends on the sintering temperature and the size of the particles. Fine-sized particles from the HEBM technique contributed to high reactivity of the particles and indirectly enhanced the driving force inside the sample. At higher sintering temperature, where grain growth occurs, the amount of porosity will be reduced, resulting in less pinning centers to the domain wall movement. Hence, the demagnetizing effect decreases and increases their magnetic permeability.

Figure 2 shows the transmittance of FTIR spectra of the YIG sintered at different temperature. The bands between 3200 and 3600 cm^{-1} should be assigned to the stretching modes of O–H bonds in yttrium/iron hydroxides. Fe_2O_3 has a corundum structure with condensed FeO_6 octahedra, which stretching vibrations is in the range of 400–500 cm^{-1} [24]. In the garnet spectrum, it is more usual to assign the bands in the IR to the Fe–O stretching vibrations of the polyhedra. The FeO_4 tetrahedra appeared at Fe–O vibration in the range of 550–650 cm^{-1} and FeO_6 octahedra appeared with the absorption range of 300–400 cm^{-1}. Thus, the lattice spectrum of the YIG consists of two groups of bands, which were assigned as YIG tetrahedral and YIG octahedral. From the IR spectra for sintering at 50–800 °C, it can be clearly seen that the peaks appeared approximately at 470, 560, and at 580 cm^{-1}. These peaks were attributed to the primary materials of the reaction Fe_2O_3, Y_2O_3 and $YFeO_3$. At 900 °C, new peaks were observable between wavenumber of 550–650 cm^{-1}, which corresponded with the YIG phase. It shows that the shifting of the peak at these wavenumber is an indicator that the garnet phase will start to form at this temperature. At 1100 °C, the YIG band became prominent. The spectrum exhibited three obvious bands at 560, 600, and 650 cm^{-1} which were assigned to the stretching mode of YIG at 1100 °C. This feature gives evident to the garnet phase formation. The spectra were very similar in wavenumber and shape to that of the YIG up to 1100 °C. However, there was a vibration band near 1680 cm^{-1}, which was associated to the deformation of O–H bonds. This was attributed to water adsorbed at the powder surface when the sample was in contact with the environment. Furthermore, it can be seen that these adsorption bands tended to become weaker with increasing sintering temperature [25, 26].

Figure 3 shows the Raman spectra of YIG in the range of 100–2500 cm^{-1} with different sintering temperature. A broader Raman signature can be observed at lower sintering temperature, for instance at 500 and 800 °C, which may be due to the small grain size or amorphous phase. For the powder sintered at 500–800 °C, it can be seen that the peak appeared at 1320 cm^{-1} which was assigned as Fe_2O_3. Other peaks at 220, 290 and 402 cm^{-1} were also attributed to the Fe_2O_3 peaks. The broad peak at 630 cm^{-1} for the sintering temperature of 500–800 °C corresponded with an intermediate phase, $YFeO_3$. With increasing sintering temperature, the peak at 630 cm^{-1} started to disappear. The peak at 380 cm^{-1} corresponded with Y_2O_3. At 900 °C, the peak at 380 cm^{-1}, characteristics of $Y_2O_{3,}$ decreased its intensity while the peak at 340 cm^{-1}, corresponded with YIG, appeared with increasing sintering temperature. It also showed the shifting of the peak at 290 cm^{-1} in the sample sintered at 800 °C–270 cm^{-1} at 900 °C, indicating that the YIG phase had started to appear. At 1100 °C, the complete YIG phase appeared as the peaks up to the 1000 °C were a more obvious feature of the garnet phase [27].

The SEM micrograph of the sintered samples shown in Fig. 4 reveals the evolution of the microstructure from lower sintering temperature to higher sintering temperature. The average grain sizes for each temperature are tabulated in Table 3. It can be seen that the average grain sizes increased with the increment in the sintering temperature.

The micrograph of the sample sintered at 500, 600 and 700 °C reveals that the sample encountered the initial stage of sintering. The initial stage of sintering involves rearrangement of the powder particles and formation of strong bond or necks at the contact point between particles. At 500 and 600 °C, the sample showed nearly the same evolution trend whereby the sample sintered at 500–600 °C showed slight particle growth and rearrangement of particles.

After sintering at 700 and 800 °C, the sample underwent the formation of necks between particles. This is indicated with the existence of dumbbell shape in the micrograph at this sintering temperature. The red-dotted circles at 700 °C indicate the necking structure between the particles. SEM micrograph of the samples sintered at 900, 1000, and 1100 °C exhibited intermediate stage of sintering. Intermediate sintering is the stage where the size of the necks grows, the amount of porosity decreases substantially and the particles move closer. At this range of temperature, grain boundaries are formed and moved so that some grains grow at the expense of others. Grain growth becomes increasingly

Fig. 2 FTIR spectra of YIG sintered at **a** 500–700 °C, **b** 800–1000 °C and **c** 1100–1400 °C

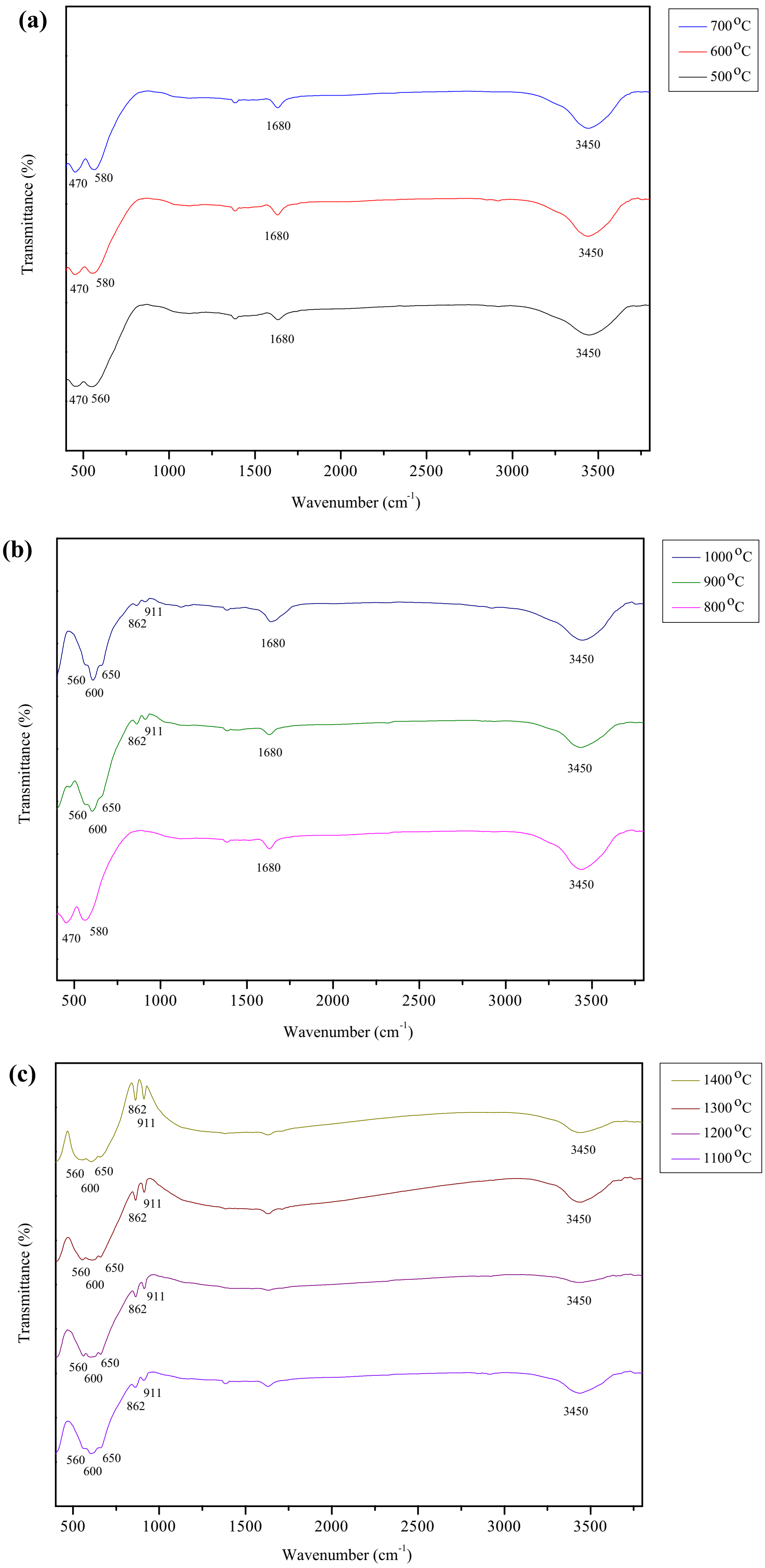

Fig. 3 Raman spectra of YIG sintered at **a** 500–700 °C, **b** 800–1000 °C and **c** 1100–1400 °C.

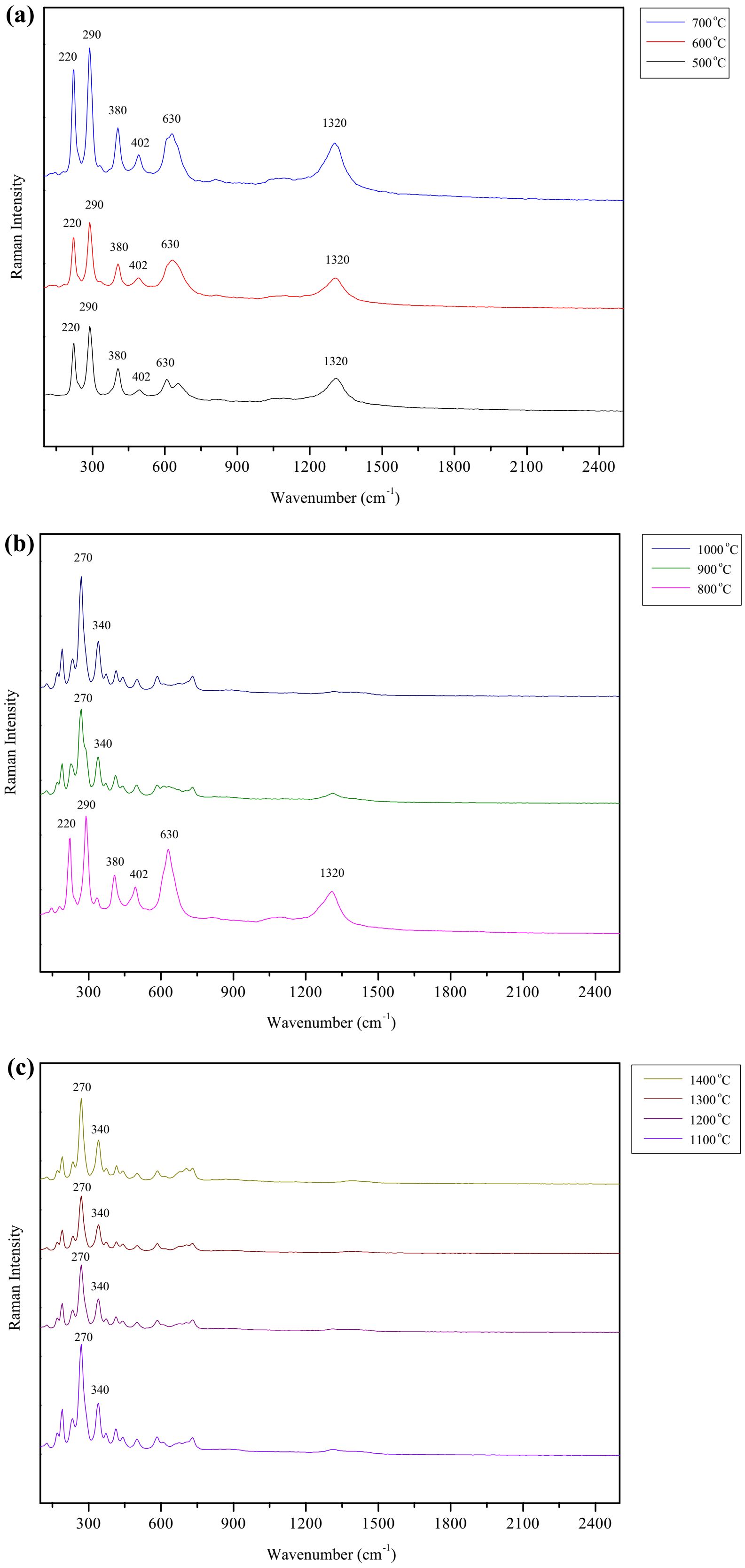

Fig. 4 FESEM micrograph at sintering temperature 500, 600, 700, 800, 900, 1000, 1100, 1200, 1300, and 1400 °C

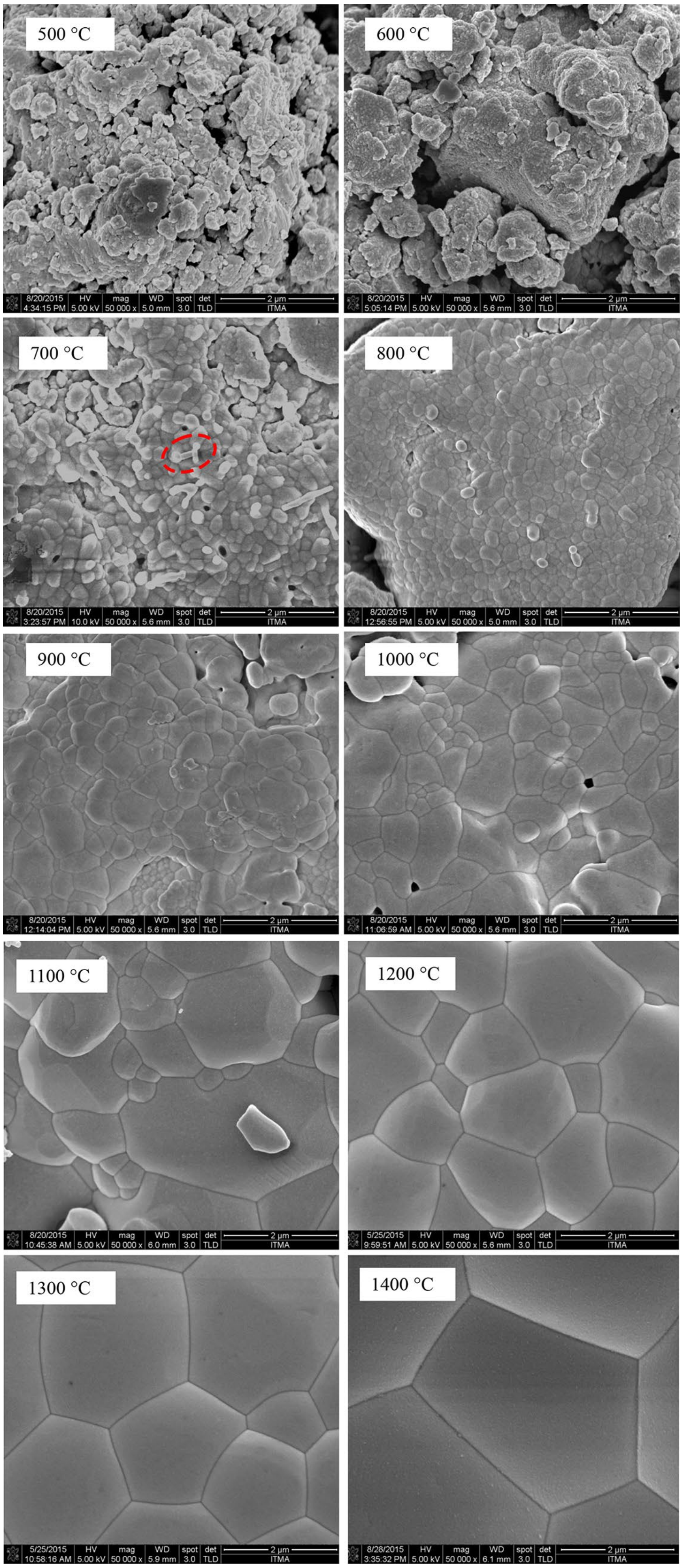

Table 3 Average grain sizes at sintering temperature of 500–1400 °C

Sintering temperature (°C)	Average grain size (μm)
500	0.032
600	0.054
700	0.182
800	0.190
900	0.331
1000	0.393
1100	0.881
1200	1.653
1300	2.841
1400	6.325

active as the pore structure collapses. The pinning effect of the pores diminishes as they shrink and occupy lesser grain boundary area.

Further sintering at 1200, 1300 and 1400 °C corresponds to the final stage of sintering. The grains with the hexagonal structure were observed in this range of temperature. At this stage, the pores diminished and were slowly eliminated by the diffusion of vacancies from the pores along the grain boundaries. The grain boundaries are regions of more open crystal structure than the grain themselves. Thus, the diffusion along grain boundary is more rapid. Reducing the grain boundary area by the grain growth lowers the energy of the system to a more stable state. From the results, it is believed that a mass transport mechanism started with atomic surface diffusion at relatively low temperature and continued to occur by the grain boundary diffusion, will result in the formation of necking, contact growth, pores elimination and grain growth.

The variation of DC resistivity values at different sintering temperatures are listed in Table 4. The resistivity was found to be increased with the increment in the sintering temperature but decreased slightly at 700 °C. YIG ideally accommodates only trivalent ions. Thus, it can be expected that the resistivity of YIG will be very high. In practice, however, the resistivity of YIG depends upon its method of preparation [10] which consequently affecting the structural and microstructure properties of YIG. Figure 5 shows the relationship found between DC resistivity and sintering temperatures. It is known that the resistivity is an intrinsic property of ferrite; thus, its crystal structure is concerned. The presence of small quantity of secondary phases may have an appreciable effect on resistivity. The comparatively low values of resistivity in samples sintered at lower temperatures, below 900 °C, are possibly due to the localized sites in the forbidden energy gap which arises due to lattice imperfections. The presence of these states effectively lowers the energy barrier to the flow of electrons [11]. However, the influence of grain boundary also affects the resistivity. Therefore, a fluctuation of resistivity values could be observed in the samples sintered between 500 and 800 °C subjected to the simultaneous existence of lattice imperfections as well as the presence of smaller grains. It may be due to the smaller grains which imply a large number of insulating grains which act as barriers to the flow of electron, thus, increasing the resistivity. With further increment in the sintering temperature from 900 to 1400 °C, the resistivity is increased. This is attributed to the better phase purity of the samples with larger grain size since electrical properties of ferrites depend upon the chemical composition as well as on the various heat treatments during the course of preparation. This behaviour can be described in terms of increasing structural improvement with increased sintering temperatures, hence improving the crystal structure, uniformity and with reduced imperfections thereby increasing the resistivity. The variation in DC electrical resistivity can be explained on the

Table 4 Resistivity at sintering temperature 500–1400 °C

Sintering temperature (°C)	Resistivity, (Ω cm)
500	1.045×10^{7}
600	3.830×10^{7}
700	1.489×10^{7}
800	4.316×10^{7}
900	1.024×10^{8}
1000	2.519×10^{8}
1100	3.340×10^{8}
1200	6.404×10^{10}
1300	7.471×10^{10}
1400	8.669×10^{10}

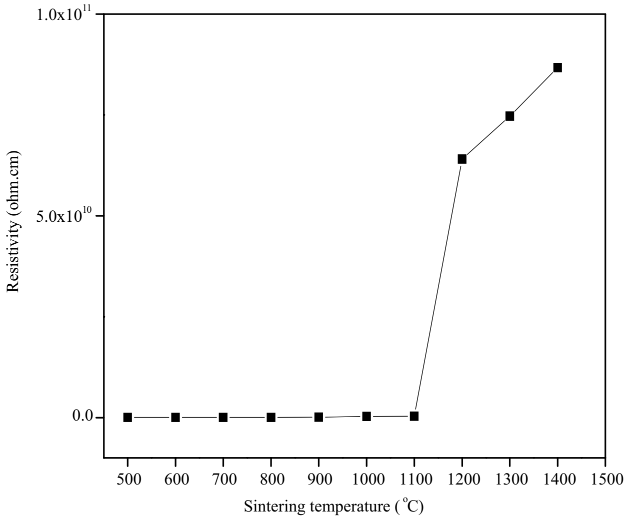

Fig. 5 Resistivity of sintered sample at sintering temperature 500–1400 °C

basis of Verwey hopping mechanism [12]. According to it, the electrical conduction in ferrites is due to the hopping of electrons between the ions of same element but of different valence states present at the octahedral sites. The conduction in ferrites is the result of hopping of electrons between Fe^{3+} and Fe^{2+} ions present at octahedral sites [13], but the occurrence are not dominant in YIG owing to its stability since in the case of garnets, all the cations are trivalent and there is no position of Fe^{2+} ions in the lattice, therefore iron garnets are essentially shown high resistivity. The highest values of DC electrical resistivity recorded from this study are in the range of 10^{10} Ω cm which is in agreement with the previous reported study by [21]. Resistivity values of YIG are usually ranged from 10^{10} to 10^{12} Ω cm [28]. The values from this study could not reach more than 10^{10} Ω cm, which still considerably high, possibly related to the sintering condition of the YIG. Since YIG in this study are sintered in the ambient air condition, some Fe^{3+} ions are expected to be reduced to Fe^{2+} ions, especially at higher sintering temperature, which are the source of hopping mechanism in ferrites even though Fe^{2+} ions concentration are low in garnets as compared to that of spinel ferrites. Generally, the electrical resistivity of ferrites decreases with the increase of temperature. This shows that ferrites have semiconductor like behaviour [29]. Ferrites have very high resistivity which is one of the considerations for microwave applications [30].

The variations of transmission loss (S_{21}) values against frequencies for various sintering temperature of YIG placed at rectangular waveguide cross section are presented in Fig. 6. As depicted from the figure, the transmission loss was increased with increasing sintering temperature. This is due to high crystallinity within the samples with larger grain size. High crystallinity indicates high purity of crystal structure resulting in a better spin contribution in high frequency range. At high frequency range, it is well known that only spin contribution dominance inside the sample. The resonance frequency is observed to shift at higher frequency as the sintering temperature increased. This phenomenon was related to the crystallographic anisotropy of the static magnetization of YIG crystals.

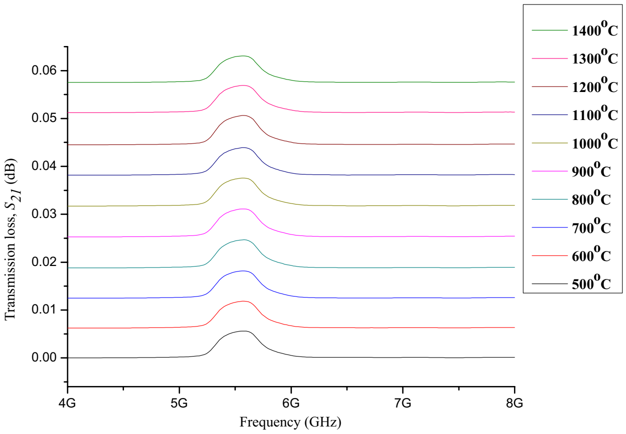

Fig. 6 The frequency dependence of the transmission loss at sintering temperature 500–1400 °C

The experimental parameter used to represent resonance losses in ferrimagnetic materials is resonance linewidth, ΔH. It is defined as the width of the resonance curve at half its transmission loss peak. For spherical sample, the resonance linewidth is measured by using the Eq. 5:

$$\Delta H = \frac{\Delta\omega}{\gamma} \tag{5}$$

where $\varDelta$ is the frequency taken from half of transmission loss peak from resonance frequency and γ is the gyroscopic ratio ($\gamma = g_B/\hbar = 1.76 \times 10^{11}\ \mathrm{T}^{-1}\ \mathrm{s}^{-1}$).

Table 5 shows the linewidth measured at 4–8 GHz as a function of sintering temperature. From Fig. 7, it can be seen that the linewidth was decreased with the increasing sintering temperature. As the grain size increased, and porosity reduced and the linewidth decreased. It is important to achieve good stoichiometry to obtain small linewidth. For this purpose, it is essential to perfectly control the regularity and reproducibility of sintering operations, as well as mixing and grinding operations.

4 Conclusion

The YIG samples were prepared using mechanical alloying with high-energy ball milling to obtain the size ranging from 32 nm to 6.325 µm. The samples were later sintered at various sintering temperature in the range of 500–1400 °C in order to study the structural, electrical and microwave properties of YIG. The XRD pattern of YIG revealed an improvement of crystallinity with the increment of sintering temperature. Full YIG phase was observed for samples sintered at 1100 °C and above. The FTIR results revealed

Table 5 Linewidth at sintering temperature 500–1400 °C measured at the frequency of 4–8 GHz

Sintering temperature (°C)	Linewidth, ΔH (Oe)
500	36.93
600	35.33
700	35.19
800	35.07
900	33.73
1000	31.00
1100	29.91
1200	27.36
1300	26.85
1400	25.61

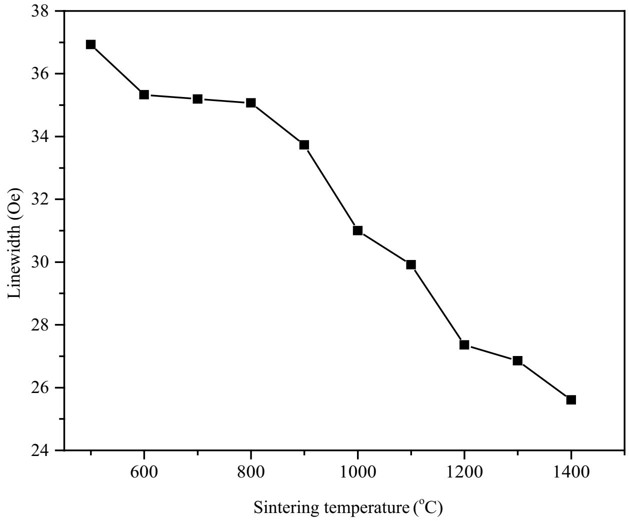

Fig. 7 Linewidth at sintering temperature 500–1400 °C measured at the frequency of 4–8 GHz

that the asymmetric stretching bond between the magnetic ions and the oxygen ions achieved was evident in the garnet phase formation. The bond shifted to a higher wave number when the sintering temperature increased. The Raman spectra confirmed that the YIG was formed at the temperature higher than 900 °C because the main peak shifted from 290 to 270 cm^{-1} and the crystalline phase of YIG appeared completely at 1100 °C. FESEM images depicted that larger grains were formed when the sintering temperature was increased, and the amount of porosity was decreased. As a result, the $YFeO_3$ phase causes the decrement in the resistivity at 700 °C and the increment of resistivity in subsequent temperatures, and this authenticated the effect of size in the purity samples. The linewidth of the sintered sample decreased with the increment of the sintering temperature as a contribution of grain size with reduced porosity.

Acknowledgements The authors are thankful to the Graduate Putra Grants UPM Malaysia Vot. Nos. 9539100 and 9541600 for its financial assistance. The authors also would like to thank the Department of Physics of the Faculty of Science, UPM and the Materials Synthesis and Characterization Laboratories (MSCL), ITMA, UPM for the measurements facilities.

References

1. D. Cruickshank, 1–2 GHz dielectrics and ferrites: overview and perspectives. J. Eur. Ceram. Soc. **23**, 2721–2726 (2003)
2. D.F. Gerald, O.E. Danial, Magnetic design for low field tunability of microwave ferrite resonators. J. Appl. Phys. **85**, 4856–4858 (1999)
3. E. Schlomann, Behavior of ferrites in the microwave frequency range. J. Phys. **31**, 443–451 (1971)
4. P.B.A. Fechine, H.H.B. Rocha, R.S.T. Moretzsohn, J.C. Denardin, R. Lavín, A.S.B. Sombra, (2009). Study of microwave ferrite resonator antenna, based on a ferrimagnetic composite (Gd3Fe5O12)GdIGx-(Y3Fe5O12)YIG1 – x. IET Microw. Antennas Propag. **3**, 1191–1198
5. I. Stanca, Magnetically tunable dielectric resonators and filters. J. Optoelectronics Adv. Mater. **6**, 59–64 (2008)
6. W.R. Holmquist, C.F. Kooi, R.W. Moss, Reaction kinetics of polycrystalline yttrium iron garnet. J. Am. Ceram. Soc. **44**, 194–196 (1961)
7. F.S. Jesus, C.A. Cortes, R. Valenzuela, S. Ammarm, A.M. Bolarin-Miro, Synthesis of $Y_3Fe_5O_{12}$ (YIG) assisted by high-energy ball miling. Ceram. Int. **38**, 5257–5263 (2012)
8. Y. Ozturk, M.F. Ebeoglugil, E. Celik, I. Avgin, Characterization of cerium-doped yttrium iron garnet films prepared by sol–gel process. Adv. Nanoscale Magn. **122**, 113–129 (2009)
9. Z. Abbas, R.M. Al-habashi, K. Khalid, Garnet ferrite ($Y_3Fe_5O_{12}$) nanoparticles prepared via modified conventional mixong oxides (MCMO) method. Eur. J. Sci. Res. **36**, 154–160 (2009)
10. S.H. Vajargah, H.R.M. Hosseini, Z.A. Nemati, Preparation and characterization of nanocrystalline misch-metal-substituted yttrium iron garnet powder by the sol–gel combustion process. Int. J. Appl. Ceram Technol. **5**, 464–468 (2008)
11. K.H.J. Buschow, *Handbook of Magnetic Materials*, 1st edn. (Elsevier B. V., Amsterdam, 2015)
12. R. Valenzuela, *Magnetic Ceramics*, 1st edn. (Cambridge University Press, New York, 1994)
13. M.N. Rahaman, *Ceramic Processing and Sintering*, 1st edn. (Marcel Dekker Inc Publication, New York, 1995)
14. R.S. Azis, M. Hashim, N.M. Saiden, N. Daud, N.N. Shahrani, Study the iron environments of the steel waste product and its possible potential applications in ferrites. Adv. Mater. Res. **1109**, 295–299 (2015)
15. A. Feng, G. Wu, C. Pan, Y. Wang, The behavior of acid treating carbon fiber and the mechanical properties and thermal conductivity of phenolic resin matrix composites. J. Nanosci. Nanotechnol. **17**, 3859–3863 (2017)
16. G. Wu, Y. Cheng, K. Wang, Y. Wang, A. Feng, Fabrication and characterization of OMMt/BMI/CE composites with low dielectric properties and high thermal stability for electronic packaging. J. Mater. Sci. **27**, 5592–5599 (2016)
17. W. Yan, W. Xinming, Z. Wenzhi, L. Chunyan, L. Jinhua, W. Yujing, Fabrication of flower-like $Ni_{0.5}Co_{0.5}(OH)_2$@PANI and its enhanced microwave absorption performances. Mater. Res. Bull. **98**, 59–63 (2018)
18. G. Wu, H. Wu, K. Wang, C. Zheng, Y. Wang, A. Feng, Facile synthesis and application of multi-shelled SnO_2 hollow spheres in lithium ion battery. RSC Adv. **6**, 58069–58076 (2016)
19. A. Feng, G. Wu, Y. Wang, C. Pan, Synthesis, preparation and mechanical property of wood fiber-reinforced poly(vinyl chloride) composites. J. Nanosci. Nanotechnol. **17**, 3859–3863 (2017)
20. C. Pan, J. Zhang, K. Kou, Y. Zhang, G. Wu, Investigation of the through-plane thermal conductivity of polymer composites with in-plane oriented hexagonal boron nitride. Int. J. Heat Mass Transf. **120**, 1–8 (2018)
21. T. Ramesh, G.N. Rao, T. Suneetha, R.S. Shinde, V. Rajendar, S.R. Murthy, S.A. Kumar, Microwave-hydrothermal synthesis of $Y_3Fe_5O_{12}$ nanoparticles: sintering temperature effect on structural, magnetic and dielectric properties. J. Supercond. Novel Magn. (2017). https://doi.org/10.1007/s10948-017-4425-6
22. N.M.M. Shahrani, R.S. Azis, M. Hashim, J. Hassan, A. Zakaria, N. Daud, Effect of variation sintering temperature on magnetic permeability and grain sizes of $Y_3Fe_5O_{12}$ via mechanical alloying technique. Mater. Sci. Forum **846**, 395–402 (2016)
23. J. Smit, H.P.J. Wijn, Ferrites. (Philips Technical Library, Eindhovan, 1959), pp. 221–245

24. C.D. Veitch, Synthesis of polycrystalline yttrium iron garnet and yttrium aluminium garnet from organic precursors. J. Mater. Sci. **26**, 6527–6532 (1991)
25. R. Chen, J. Zhou, L. Zheng, H. Zheng, P. Zheng, Z. Ying, J. Deng, Two-step sintering behavior of sol–gel derived dense and submicron-grained YIG ceramics. J. Electron. Mater. (2018). https://doi.org/10.1007/s11664-018-6080-5
26. M.A. Musa, R.S. Azis, N.H. Osman, J. Hassan, T. Zangina, Structural and magnetic properties of yttrium iron garnet (YIG) and yttrium aluminum iron garnet (YAlG) nanoferrite via sol-gel synthesis. Results Phys. **7**, 1135–1142 (2017)
27. R. Nazlan, M. Hashim, I.R. Ibrahim, F.M. Idris, W.N.W.A. Rahman, N.H. Abdullah, I. Ismail, S. Kanagesan, Z. Abbas, R.S. Azis, Influence of indium substitution and microstructure changes on the magnetic properties evolution of $Y_3Fe_{5-x}In_xO_{12}$ ($x = 0.0$–0.4). J. Mater. Sci. **26**, 3596–3609 (2015)
28. A. Goldman, (2006) *Modern Ferrite Technology*. (Springer Science and Business Media, Inc., Pittsburgh)
29. T.A. Ring, *Fundamentals of Ceramic Powder Processing and Synthesis*, 1st edn. (Academic Press. Inc. Publication, New York, 1996)
30. H.M. Widatallah, C. Johnson, S.H. Al-Harthi, A.M. Gismelseed, A.D. Al-Rawas, S.J. Stewart, M.E. Elzain, I.A. Al-Omari, A.A. Yousif, A structural and mössbauer study of $Y_3Fe_5O_{12}$ nanoparticles prepared with high energy ball milling and subsequent sintering. Hyperfine Interact. **183**, 87–92 (2008)